Fall 1-27-2008

Fully dense aluminum-rich aluminum copper oxide powders for energetic formulations

Demitrios Stamatis
New Jersey Institute of Technology

ABSTRACT

FULLY DENSE ALUMINUM-RICH ALUMINUM COPPER OXIDE POWDERS FOR ENERGETIC FORMULATIONS

by
Demitrios Stamatis

The thermite reaction between Al and CuO is well known and highly exothermic. For a conventional thermite mixture comprising mixed metal and oxide powders, this reaction is rate limited by the slow heterogeneous mass transfer at the metal and oxide interface. The relatively low reaction rate and a difficult ignition have restricted practical applications for this reaction. For newly developed, nano-composed thermites, the interface area can be substantially increased resulting in a much higher reaction rate and a new range of possible applications. Nanocomposite Al-CuO materials are produced using a technique referred to as arrested reactive milling. Regular metal and oxide powders are blended and ball milled at room temperature resulting in a fully dense and reactive nanocomposite powder. The produced Al-CuO nanocomposite powders have been considered for applications in propellants, explosives, pyrotechnics, as well as for joining small parts. In accordance to the application requirements, the powder composition and morphology can be modified to optimize performance. Aluminum-rich compositions are of particular interest for novel energetic components. Synthesis methodology, material properties as a function of composition and morphology, and performance tests will be discussed in this paper.

FULLY DENSE ALUMINUM-RICH ALUMINUM COPPER OXIDE POWDERS FOR ENERGETIC FORMULATIONS

by
Demitrios Stamatis

A Thesis
Submitted to the Faculty of
New Jersey Institute of Technology
in Partial Fulfillment of the Requirements for the Degree of
Master of Science in Mechanical Engineering

Department of Mechanical Engineering

January 2008

APPROVAL PAGE

FULLY DENSE ALUMINUM-RICH ALUMINUM COPPER OXIDE POWDERS FOR ENERGETIC FORMULATIONS

Demitrios Stamatis

Dr. Edward L. Dreizin, Thesis Advisor — Date
Professor of Chemical Engineering, NJIT

Dr. Boris Khusid, Committee Member — Date
Professor of Chemical Engineering, NJIT

Dr. Kwabena Narh, Committee Member — Date
Associate Professor of Mechanical Engineering, NJIT

Dr. Mirko Schoenitz, Committee Member — Date
Research Professor of Chemical Engineering, NJIT

BIOGRAPHICAL SKETCH

Author: Demitrios Stamatis

Degree: Master of Science

Date: January 2008

Undergraduate and Graduate Education:

- Master of Science in Mechanical Engineering,
  New Jersey Institute of Technology, Newark, NJ 2008

- Bachelor of Science in Mechanical Engineering,
  New Jersey Institute of Technology, Newark, NJ 2006

Major: Mechanical Engineering

Presentations:

Demitrios Stamatis, Zhi Jiang, Vern K. Hoffmann, Mirko Schoenitz, and Edward L. Dreizin,
"Fully Dense AlCuO Nanocomposite Powders for Energetic Formulations,"
American Institute of Chemical Engineers National Conference 2007,
Salt Lake City, UT, November 2007.

Demitrios Stamatis and Edward L. Dreizin,
"Fully Dense AlCuO Nanocomposite Powders for Energetic Formulations,"
AIAA Region 1-NE Student Conference
MIT, Cambridge, Massachusetts, April 2007.

Dedicated to the Lord, for without his strength and mercy, I cannot be or do.

ACKNOWLEDGMENT

I would like to very much thank Dr. Edward Dreizin for his patient and concerned guidance in my research and academic progress. I could not ask for a better advisor. Special thanks are given to Dr. Boris Khusid, Dr. Kwabena Narh, and Dr. Mirko Schoenitz for participating on my thesis committee. I would like to acknowledge my sponsors TACOM-ARDEC, Picattiny, and the Defense Threat Reduction Agency. Many thanks go to Mr. Vern Hoffman for his help in the lab, and also to Dr. Mirko Schoenitz for his continuous help and assistance in pretty much everything. I also thank my lab mates, Ervin Beloni and Salil Mohan for their advice and friendship. Most of all, I thank my family who have supported all my decisions and actions. Through their hard work and suffering, I am able to enjoy the privilege of higher education.

TABLE OF CONTENTS

TABLE OF CONTENTS
(Continued)

LIST OF TABLES

LIST OF FIGURES

LIST OF FIGURES
(Continued)

CHAPTER 1

INTRODUCTION

1.1 Objective

The goal of this project was to develop fuel rich Al-CuO nanocomposite powders with focus on applications in formulations for enhanced blast explosives. Synthesis conditions were to be determined to produce the powder performing best in ignition and combustion experiments. Both powder bulk composition and specific synthesis parameters were considered as experimental variables. A methodology was to be developed to characterize the produced nanocomposite materials. The correlations of materials characteristics with its improved ignition and combustion performance were to be studied and documented for each prepared sample. Based on such correlations, the conclusions were to be made about the mechanisms of improved ignition and combustion performance. The materials characteristics were to be classified as those having strong or weak correlations with the ignition and combustion performance. An additional project objective was to evaluate the feasibility of using the same fuel-rich Al-CuO nanocomposite powders as a reactive filler material for joining small copper plates. The effect of powder composition and other parameters on the quality of the obtained joint was to be determined.

1.2 Background

Metal-based energetic materials are finding applications in propellants, explosives, and pyrotechnics [1-2]. The main advantage of using these materials is their high reaction enthalpy exceeding that of hydrocarbon based energetics. The limiting factors of using these energetic materials are their low reaction rates, long ignition delays, and incomplete burning. For example, long ignition delays cause agglomeration of molten aluminum particles in solid propellants [3]. New developments have led to reactive metal-based nanomaterials [4-10]. The main idea is to greatly increase the surface area leading to an increase in reaction rate and a decrease in ignition delay.

There are two production approaches used to create the nanocomposite materials. A more common, bottom-up approach is based on nano-particles or nano-foils produced from elemental atoms or molecules. One bottom-up technique includes mixed metal-metal oxide nanoparticles (termed metastable intermolecular composites or MIC) [4-5]. One method of producing the nano-sized aluminum particles is the wire explosion technique. The particles are produced by passing high current through the metal wire in an inert atmosphere. The high current causes the wire to melt and boil via superheating. The vapor is cooled into small particles and generally collected through some type of gas stream. In the wire explosion technique the particle size is controlled by the superheating of the metal wire. In the MIC technique, nanoparticles of metal and metal oxides are suspended in a hexane solution and mixed through sonication. The sonication process helps to break up agglomerates which are formed due to the agglomerating nature of nanoparticles.

Another technique is referred to as sol-gel processing [7]. In this technique a solid matrix of oxidizer particles is built, where the fuel is embedded into the pores. A stable sol is formed by dissolving the molecular precursors of an oxidizer, which then undergoes hydrolysis and condenses. The sol is further linked by condensation of surface groups on the particle surface to form a gel, which is a rigid nano-structured frame having nano-sized pores. The pore fluid is then removed by either evaporation or supercritical extraction and results in a xerogel or aerogel respectively.

Layering of reactive components is another technique that unlike other bottom-up approaches results in a nano-foil rather then a powder [8-9]. Magnetron gun sputtering is used to deposit alternating layers of fuel and oxidizer on a substrate. The thickness of the layer can be controlled to allow tailoring of the combustion process. This type of nanocomposite has found use in joining applications.

The top-down approach used in this research is based on refining the bulk materials to achieve nano-scaled mixing between components. A related practical technique is called arrested reactive milling (ARM) [10-15]. ARM is based on high energy mechanical milling whereby starting components of regular micron-sized powders capable of highly exothermic reaction are ball milled together. ARM is derived from reactive milling where powders capable of an exothermic reaction are ball milled. In material systems of high reaction enthalpy, the reaction becomes self sustained after being mechanically triggered during milling. In ARM, the mechanically initiated exothermic reaction is prevented by arresting (or stopping) the milling when the desired powder refinement is achieved. The product is a metastable, fully dense, highly-reactive nanocomposite powder. The mixing takes place at the nanoscale level, while the particle

sizes are in the micron-range. Therefore, each micron-sized particle represents a nanocomposite structure of reactive components.

Systems of interest include metal-metal composites such as Al-Ni and Al-Ti, metal-metalloid composites such as Ti-B, Zr-B, and metal-oxide composites, such as Al-MoO3, Al-CuO, and others. This research focuses on the particular system of Al-CuO for potential applications in pyrotechnics, explosives, propellant additives, and for joining/welding of small components. Metal-rich compositions were explored to take advantage of external oxidizers, such as air for explosives or ammonium perchlorate for propellants. Metal-rich composites can also provide more metal to form filler necessary to achieve better structural or strength properties for joining applications.

The materials prepared in this project were specifically considered for two applications: joining and enhanced blast explosives. The focus of this project was to investigate whether shifting composition of nanocomposite Al-CuO thermite system towards the Al-rich end would allow one to maintain the high reaction rates, similar to those observed for stoichiometric compositions. The synthesis conditions appropriate for metal-rich materials were determined by varying synthesis parameters and observing their effects on the product powder. The powders were characterized by particle size, internal macro-structure (inclusion shapes and sizes), composition, reaction kinetics, and ignition and combustion performance. The material's characteristics were then correlated to the improved ignition and combustion behavior. The fuel-rich materials were also used in the joining experiments for bonding of fiberglass plates covered with copper foil.

1.3 Arrested Reactive Milling

The nanocomposite powders used in all the experiments were prepared by ARM. Materials used for ARM synthesis are capable of highly exothermic reactions between one another. The material system in this case belongs to a group of thermites, such as Al-Fe_2O_3, Al-CuO, or Al-MoO_3. During the ball milling of starting components, such as Al and CuO, the reaction can be triggered mechanically and becomes self-sustaining. This kind of reaction usually proceeds rapidly resulting in a significant increase in the temperature of the milling vial. Figure 1.1 shows the temperature as a function of time for a milling vial in which a thermite system is being processed. The mechanically triggered reaction can be observed by the temperature spike. In ARM, the milling is arrested just before the reaction is triggered. The resulting powder is a fully dense and highly reactive metastable nanocomposite.

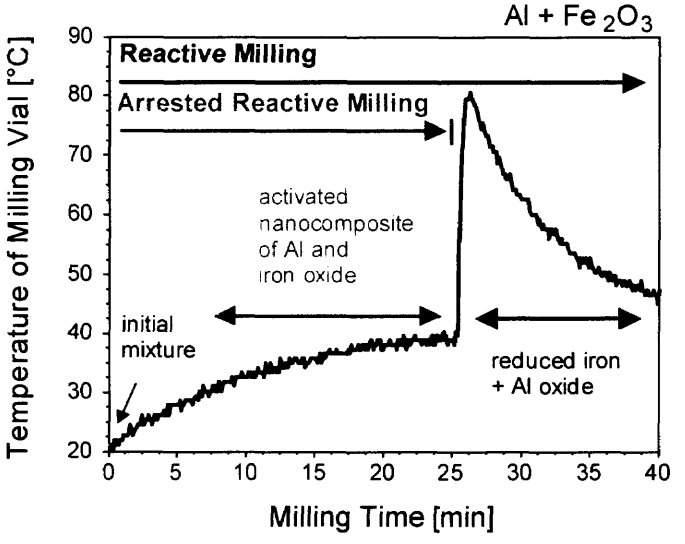

Figure 1.1 Temperature of milling vial as a function of milling time.

1.4 Thermite for Joining Applications

The thermite mixture is most commonly used today in welding of railroad tracks [23-24]. The parts to be welded are enclosed in a sand mold. The thermite mixture, in this case aluminum and iron(III)oxide are place in a crucible on top of the mold. The mixture is ignited and the reaction proceeds with the aluminum oxidizing and resulting in pure molten iron. The molten iron flows out of the crucible through an opening and fills the sand mold and joins the railroad track. In this project, the traditional process is modified by not using a mold and instead forming the thermite material into a pellet to be place between the parts to be joined.

CHAPTER 2

EXPERIMENTAL

2.1 Material Preparation

Aluminum used was provided by Atlantic Equipment Engineers, -325 mesh (45 μm), 99.5% pure. Copper oxide was provided by Sigma-Aldrich (26 μm), 99+% pure, pre-milled Sigma-Aldrich (1.5 μm), and also Alfa Aesar, 30-50 nm. Milling medium, in this case 10 mm steel balls made of AISI/SAE 1013 low-carbon steel, are added with a ball to powder mass ratio (BPR) of 3. Hexane was added as a process control agent to prevent cold welding and partial reaction of the powders during their processing. Milling was performed using the Retsch 400PM planetary mill as shown in Figure 2.1.

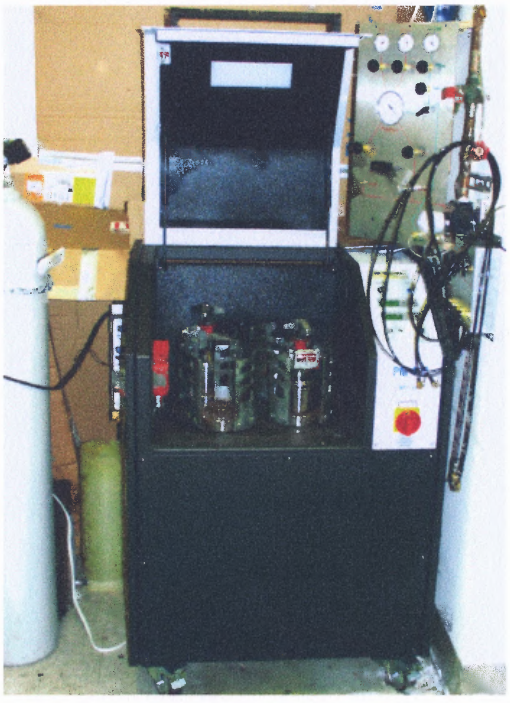

Figure 2.1 Picture of the planetary mill.

The rotation speed was set to 350 RPM. The mill was set to reverse direction of rotation every 15 minutes. The vials used were custom made steel jars designed for high pressure applications as shown in Figure 2.2. The steel vials had the following dimensions: ID 64mm x 52mm 18mm wall thickness.

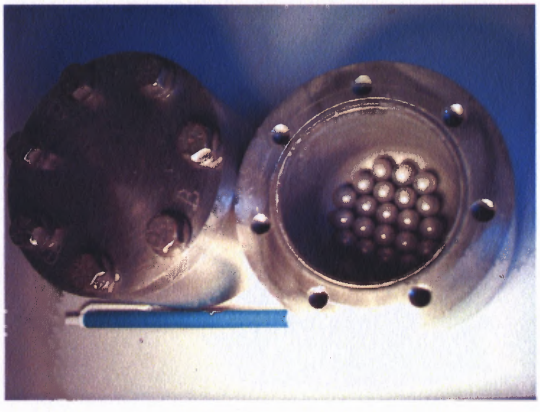

Figure 2.2 Picture of high pressure steel milling vials.

The mill was air-conditioned to maintain the milling compartment at the temperature of 19 °C. The temperatures of the vials were monitored using wireless temperature sensors (Point Temperature Sensors including 418 MHz transmitters by Point Six Wireless, Inc.) as shown in Figure 2.3.

Figure 2.3 Picture of wireless temperature sensor on milling vial.

The high energy milling can mechanically initiate the reaction. Therefore, the milling is arrested just before this reaction can occur. The time of arrest is determined based on earlier experiments and based on the estimated parameter called milling dose and indicating the degree of processing achieved [10].

2.2 Parametric Study of Synthesis

The stoichiometric composition is identified as 2Al+3CuO, whereas the fuel-rich composition is identified as xAl+3CuO, with $x > 2$. In this study 8, 10, and 12 are used for x. Several milling parameters can be varied to control the properties of the milling product. These include powder load, ball load, milling time, milling speed, and PCA type and amount. In this project, milling time and PCA amount were parametrically varied. In addition, different copper oxide powders were used. The powder load, 30g per vial, ball to powder ratio (BPR) 3, and the milling speed, 350 rpm, were kept constant. The samples are identified by moles of aluminum and milling conditions (mc). For example, 8mc-0s is the 8Al+3CuO composition made using 15 mL hexane and 60 minute milling time using regular Sigma-Aldrich copper oxide. The pre-milled Sigma-Aldrich copper oxide powder is noted by a 'p' and the Alfa-Aesar powder denoted by 'n'. Table 2.1 lists the sample ID's and respective different conditions used in the study. The pre-milled CuO powder was prepared by milling the copper oxide with steel balls using BPR of 3 with no PCA for 30 minutes in the same custom made high pressure milling vials at 350 rpm.

Table 2.1 Parameters of Materials Synthesis

Sample ID	CuO type	Measured CuO size, μm	PCA, mL Hexane	Milling Time, min
8mc-0s	Sigma-Aldrich	26	15	60
8mc-1s	Sigma-Aldrich	26	24	60
8mc-2s	Sigma-Aldrich	26	24	120
8mc-0p	Sigma/pre-mill	1.3	15	60
8mc-1p	Sigma/pre-mill	1.3	24	60
8mc-1n	Alfa Aesar	0.03 – 0.05*	24	60
8mc-3n	Alfa Aesar	0.03 – 0.05*	48	60
10mc-1s	Sigma-Aldrich	26	24	60
12mc-1s	Sigma-Aldrich	26	24	60

*Nominal size

2.3 Characterization

Particle size distributions (PSD) for the prepared nanocomposite powders were measured using the Coulter LS230 low-angle laser light scattering particle size analyzer. De-ionized water was used for the suspension of particles.

Prepared nanocomposite powders were also characterized using scanning electron microscopy. For SEM analyses, a LEO 1530 Field Emission Scanning Electron Microscope operating at 10 kV was employed. Back-scattered electron imaging was used to obtain images showing the phase contrast between the materials.

The samples were prepared by pouring a small amount of powder into a 10 mm plastic test tube. Then, an epoxy was made by mixing resin and hardener and poured over the powder in the test tube. The test tube was then placed in a centrifuge for 30 minutes to remove air trapped in the powder. The epoxy was allowed to harden over a

period of 1-2 days. The tip of the test tube would then be cut off and the powder inside the tip would come out in a solid piece due to the epoxy binder. The sample was then placed into a pre-drilled hole in a brass block and covered in epoxy. After, the epoxy dried, the surface of the brass block was wet sanding using up to 1200 grit sandpaper in order to achieve a smooth surface cross-section. A silver solution was used to connect the cross-sectioned sample surface to the bronze block. The high conductivity of the brass helped reduce surface charge of the sample and result in increased resolution images.

X-ray diffraction was used to determine phase composition for each sample. The XRD was performed on a Philips X'pert MRD powder diffractometer operating at 45 kV and 40 mA using Cu Kα radiation (λ = 1.5438 Å). Scan angle was in the range of 30-50 degrees for as milled powders and 10-90 degrees for combustion products.

Reactions occurring in the produced powders were characterized by differential scanning calorimetry (DSC) using a Netzsch STA409PC thermal analyzer. The measurements were performed in argon with a heating rate of 10K/min. Alumina sample pans covered with lids were used. And the DSC furnace was flushed with argon at approximately 20 ml/min. The temperature range was limited to a maximum of 1000 °C. After the initial heating cycle, the sample was cooled to room temperature, and then re-heated again at the same heating rate to obtain a baseline for the measurement. It was assumed that the bulk heat capacity of the sample did not change dramatically between the first and second heating.

2.4 Ignition Temperature and Kinetics

The ignition performance of the powders was characterized using filament ignition apparatus [16]. Figure 2.4 shows a simplified schematic of the filament ignition setup.

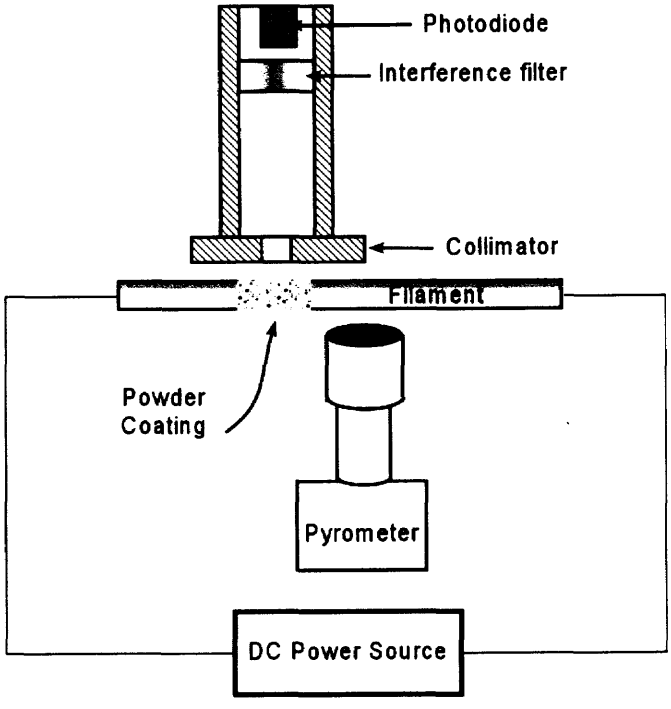

Figure 2.4 Schematic diagram of filament ignition apparatus.

A 0.5mm diameter Chromel wire mounted in the experimental chamber was used as the filament. The wire from the spool is stretched in order to straighten it. To account for thermal expansion of the wire during heating, one of the electrodes is attached to a linear slide with a tensioning spring. A gauge is used to set the wire length to 4.67 cm each run. A small amount of powder was mixed with hexane to form slurry and this slurry was applied to a small section of the filament about 1 cm as a thin layer using a soft brush. A gauge is again used to correctly place the layer of powder each run which is fully dried before heated. One to three car batteries connected in series provided the DC current through the filament. A resistor network, included together with the batteries

into the DC power source shown in Figure 2.4, allowed for different configurations of resistors in order to vary the heating rate of the filament. Heating rates used varied from 10^2 to 10^4 K/s. Ignition was observed using a silicon photodiode (DET110 by Thorlabs, Inc.) equipped with an iris aimed at the powder coating from a distance of 4-5 cm. The temperature history of the heated filament was measured using a high-speed infrared pyrometer (DP1581 by Omega Engineering, Inc.). The pyrometer was focused on the uncoated surface of the filament adjacent to the powder coating. The pyrometer was calibrated using a Blackbody Calibrator (BB-4A) from Omega Engineering, Inc. in the temperature range between 800 and 1250 K.

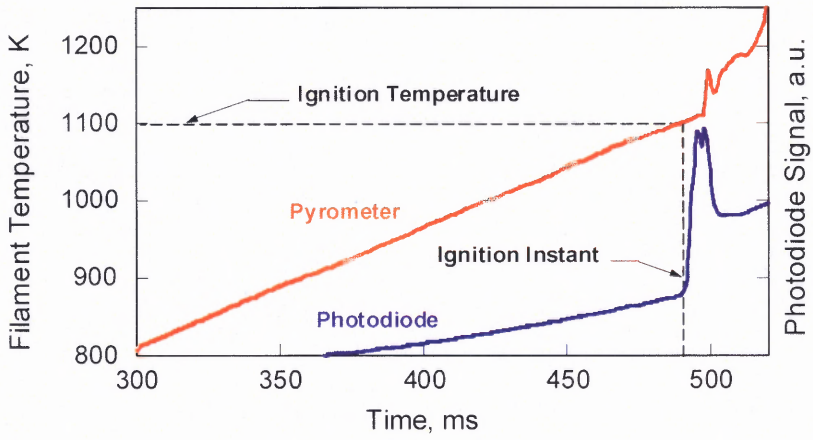

Figure 2.5 Sample traces of photodiode and pyrometer signals.

Figure 2.5 shows a sample trace from a typical run. The moment of ignition is taken as the point where there is a sharp increase in the photodiode signal. At the corresponding time, the ignition temperature is taken from the pyrometer trace. The filament ignition experiment can be conducted in either an air or argon environment. The change in the ignition temperature as a function of the heating rate is used to describe ignition kinetics.

2.5 Combustion Performance

The combustion performance of the prepared nanocomposite powder was studied using the constant volume explosion experiment [17-21]. Figure 2.6 shows a schematic of this experiment.

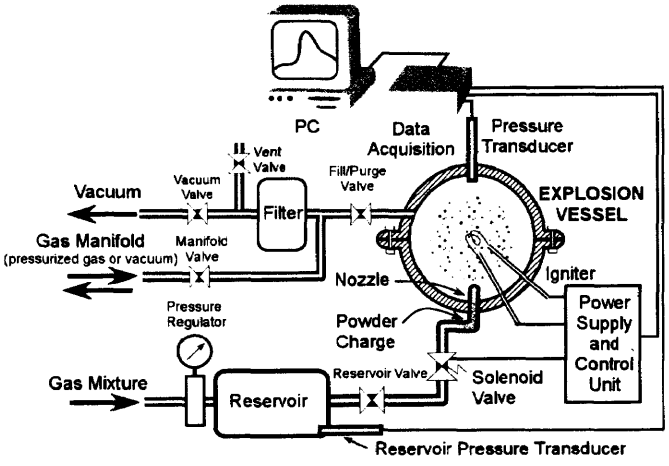

Figure 2.6 Schematic of the constant volume explosion experiment.

The combustion parameters of the prepared nanocomposite powders were compared to those of reference aluminum powder. The experimental methodology is based on a technique developed by the U.S Bureau of Mines for characterization of explosibility of various dusts. A 9.2 L explosion vessel was used. The vessel was initially evacuated. The mass load for aluminum powder was selected to achieve the maximum explosion temperature based on the thermodynamic calculations performed for the experimental vessel volume. For the 9.2 L vessel filled with air at 1 atm, the constant volume calculation using the NASA's CEA program predicted an aluminum load of 2.89 g, which was used in the experiments. The results of the software calculations are shown in Figure 2.7.

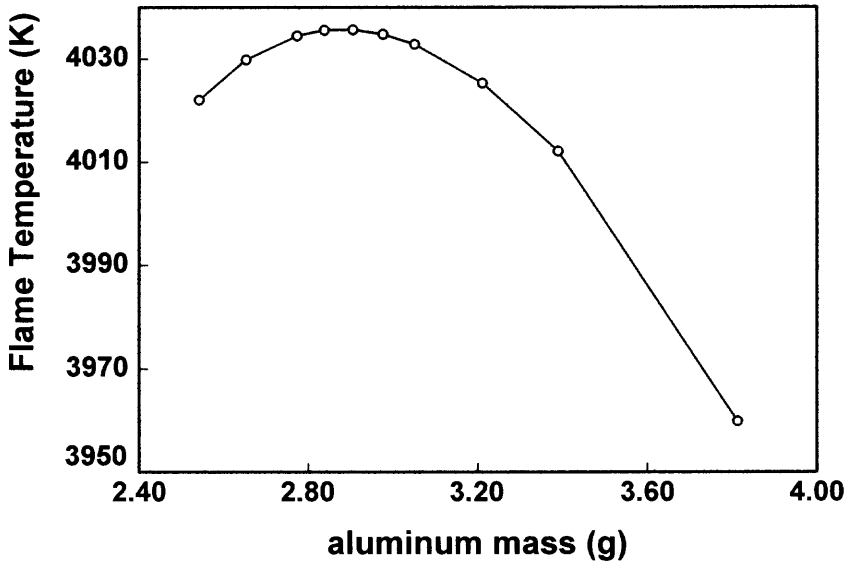

Figure 2.7 Calculation of flame temperature vs aluminum loading.

The load of the nanocomposite powder was selected to match the volume of the aluminum powder load. The nanocomposite loads and their respective aluminum content are shown in Table 2.2.

Table 1.2 CVE Loading Amounts

Composition	Load, g	Aluminum Content, g	% Al by mass
Al powder	2.89	2.89	100
8Al3CuO	4.10	1.95	47.5
10Al3CuO	3.95	2.09	52.9
12Al3CuO	3.80	2.19	57.6

For the nanocomposite powders, the mass load was calculated by finding the volume of the aluminum powder, corresponding to the maximum adiabatic flame temperature predicted by CEA code and multiplying it by the calculated theoretical maximum density of the nanocomposite.

A short gas blast delivered from a high pressure reservoir through a nozzle with multiple small openings introduced powder into the evacuated vessel and simultaneously

established the initial gas environment and pressure for the ensuing combustion. After a short delay, necessary to minimize initial turbulence in the vessel, aerosolized powder was ignited by a heated filament placed in the center of the vessel. The pressure was monitored in real time using a pressure transducer. All the experiments were performed in dry air. The final operating parameters were as follows: gas blast duration: 500 ms, the reservoir pressure: 2.45 atm, initial pressure in the explosion vessel prior to ignition: 1 atm, delay between the gas blast and ignition: 300 ms.

2.6 Joining Experiment

The joining of small parts was attempted as shown in Figure 2.8. A small vise was used to contain the components to be joined and the filler material. The two parts to be joined were simply fiberglass plates with thin copper foil layers on each side. The dimensions of the plates were about 10 mm x 10 mm x 2.3mm. The material was formed into a pellet using a custom made three piece metal mold and die that is held together using two bolts. The cross section in the mold is 10 mm x 9 mm.

A procedure was developed to create consistent pellets and allow systematic variation of the parameters. The first step was to cut a copper foil covered fiberglass plate of 9 mm x 8 mm cross section and place this at the bottom of the mold. This would later assist in extraction of the pellet. The desired mass of powder was weighed using a digital scale and placed into the mold. The mold was then given a tapping on a hard surface to distribute the powder evenly on the bottom. The die was then placed into the mold and then the mold was placed into the center of the hydraulic press. Two types of presses were used. The stoichiometric composition pellet was made in a press whose

gauge read in pound force. The aluminum rich composition pellets were made using model 16T MTI corporation press whose gauge read in MPa. The press was then manually pumped to pressure varying from 10000 to 12000 lbs compressive force or 10 to 20 MPa pressure as indicated by the pressure gauges of the respective press model. Having a three part mold that could be disassembled aided in the extraction of the pellet. The pellet was then weighed again on the digital scale and the thickness was measure using a digital caliper.

The thermite pellet was sandwiched between these two fiberglass plates. A stiff spring was used to apply force and hold the assembly in place upon ignition. The compressive force is important to counteract the gas release that can occur upon ignition and push the plates apart. The reaction was initiated using an electrically heated tungsten wire. A Panasonic digital video camera was mounted to record the reaction progress. The joined parts were recovered and cross-sectioned. The cross-sections were examined using SEM in order to evaluate the quality of the produced bonding.

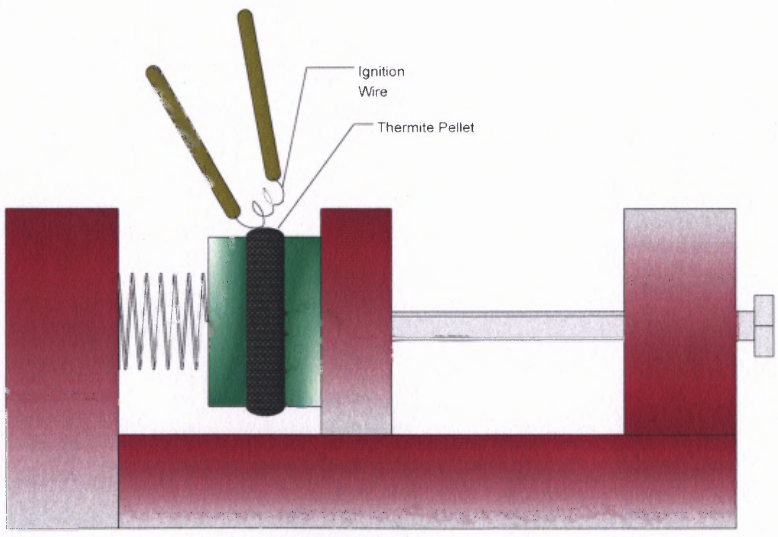

Figure 2.8 Schematic describing setup of joining experiment.

The list of pellets made using stoichiometric compositions is shown in Table 2.3, where mass and compressive forces were varied under the assumption that density and mass would affect the performance. Table 2.4 lists the pellets made using the aluminum rich compositions of 8, 10, and 12 mol aluminum.

Table 2.3 Table of Different Thermite Pellet Samples Made Using Stoichiometric Composition

Sample	Mass, g	Compression Force, lb	Pellet Thickness, mm	Pellet Density, g/cc
1	0.14	10,000	0.60	3.07
2	0.10	10,000	0.50	2.63
3	0.06	11,000	0.39	2.02
4	0.10	10,000	0.40	3.28
5	0.09	12,000	0.46	2.57
6	0.08	12,000	0.28	3.75
7	0.09	12,000	0.35	3.38
8	0.09	12,000	0.42	2.81

Table 2.4 Table of Different Thermite Pellet Samples Made Using Aluminum Rich Composition

Sample	Compression Force, MPa	Composition
1	10	8Al+3CuO
2	10	8Al+3CuO
3	10	8Al+3CuO
4	10	8Al+3CuO
5	20	8Al+3CuO
6	20	8Al+3CuO
7	20	8Al+3CuO
8	20	8Al+3CuO
9	10	10Al+3CuO
10	10	10Al+3CuO
11	10	10Al+3CuO
12	20	10Al+3CuO
13	10	12Al+3CuO

CHAPTER 3

RESULTS AND DISCUSSION

3.1 Particle Size Distributions

The measured size distributions of the starting powders (except for the nanopowder) are shown in Fig. 3.1. Both commercial Al and micron-sized CuO powders are clearly size classified based on a sharp cut-off in the size distribution on the side of coarse particles. The pre-milling step results in a remarkable particle size reduction of the commercial CuO powders.

Figure 3.2 shows particle size distributions of the 8Al+3CuO nanocomposite powders prepared with different milling conditions. For most samples, the size distributions extend to larger particle sizes, as compared to the size distributions of the starting powders shown in Fig. 3.1. The formation of larger particles can be seen as an indicator of the formation of composite materials. From that standpoint, the size distribution for the 8mc-1p sample is somewhat alarming. It ends sharply at around 40 - 50 μm, as does the original Al powder size distribution. This sample used pre-milled CuO powder and the shape of the size distribution function for the product powder indicates that formation of composite particles was limited. For a sample with the same starting materials but milled with less PCA (8mc-0p) the formation of larger particles is already observed as for other samples.

A longer milling time (sample 8mc-2s) results in the formation of a PSD function that approaches the lognormal distribution. This shape of PSD is expected to be maintained at even longer milling times. The PSD of the powder milled for a shorter time but with less PCA (8mc-0s) is also fairly close to the lognormal shape, indicating a

greater rate of particle size modification as compared to the similar conditions, but with more PCA (8mc-1s).

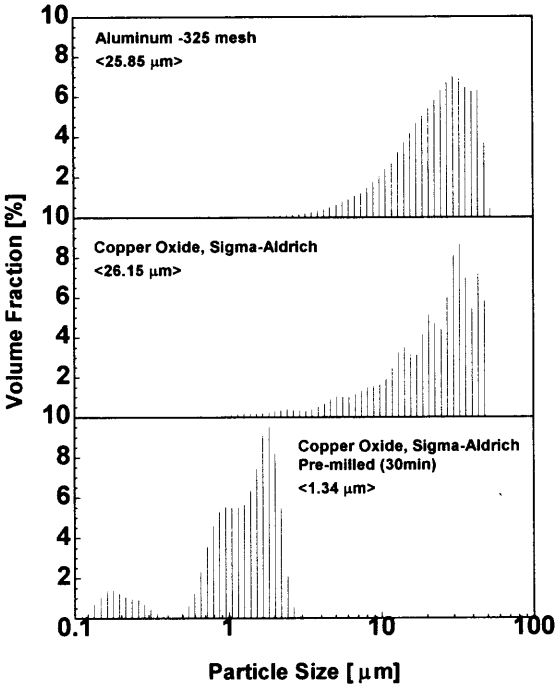

Figure 3.1 Particle size distributions of starting materials.

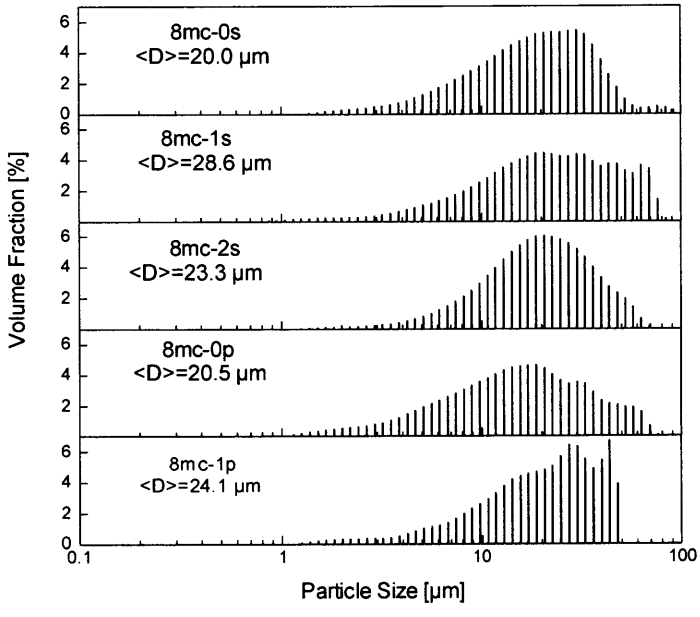

Figure 3.2 Particle size distributions of various milling conditions.

Figure 3.3 shows the PSD of the three different aluminum compositions using the same milling condition (24 mL of PCA and 60 min milling time). It can be seen that increasing aluminum content increases the amount of coarse particles and decreases the amount of fines. This is the expected behavior since aluminum is soft and malleable. The mean sizes on the other hand do not have an apparent trend. It would be expected that the mean size would increase with increasing aluminum content as well. This is not the case since the 8 and 12 mol compositions have almost the same mean sizes, whereas the mean size for the 10 mol composition is somewhat greater. Repeated size analyses showed that this result was reproducible.

In general, the differences in the PSD shapes corresponding to different milling conditions are minor.

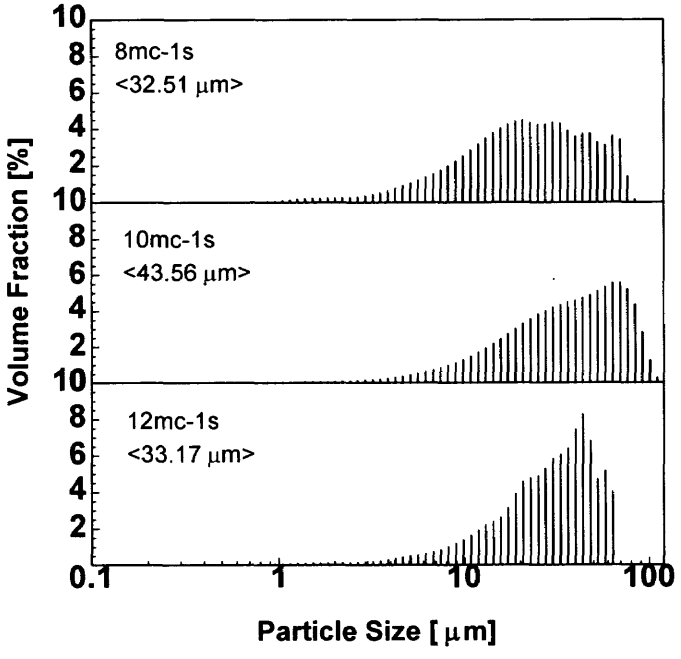

Figure 3.3 Particle size distributions of different compositions.

3.2 Morphology

Typical cross-sections of 8Al+3CuO nanocomposite particles imaged using SEM are shown in Figure 3.4. In this low magnification image the particles are of irregular shape and of micron sized diameters. The particles range in size from less than 10 microns to 100 microns. Figure 3.5 shows a higher resolution image where the nanoscale mixing can be seen in detail within a selected particle. The black background is the epoxy, the light colored area indicate the denser copper oxide inclusions and the gray areas show the less dense aluminum matrix. From these images it can be seen that the copper oxide is fully mixed into the aluminum and the particles are fully dense. In Figure 3.4 a large flat particle is seen that has length of about 400 microns. This particle is still a nanocomposite and the copper oxide is fully mixed within. Particles such as these are formed due to agglomeration and cold welding during the milling process. According to the PSD of the starting materials, no particles of this size are present. Therefore, it is concluded that this particle was formed during the milling process.

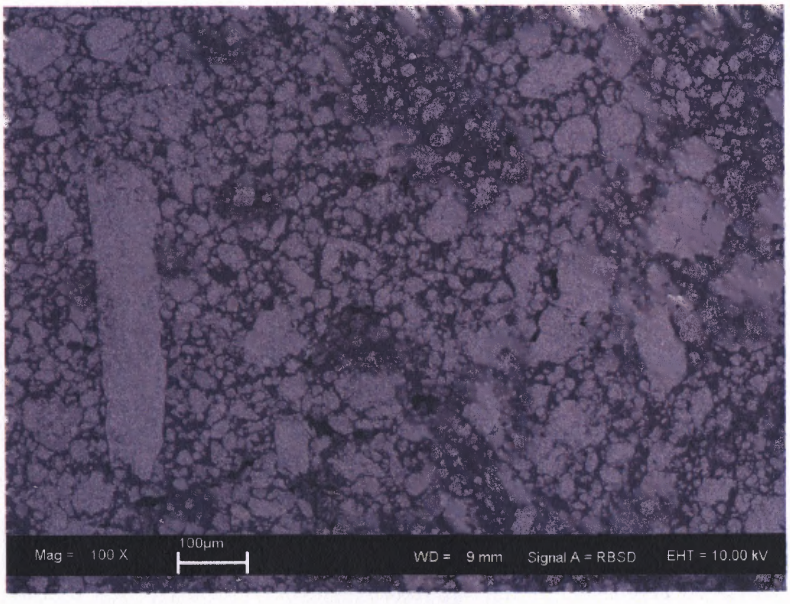

Figure 3.4 Low magnification image of typical 8Al+3CuO nanocomposite.

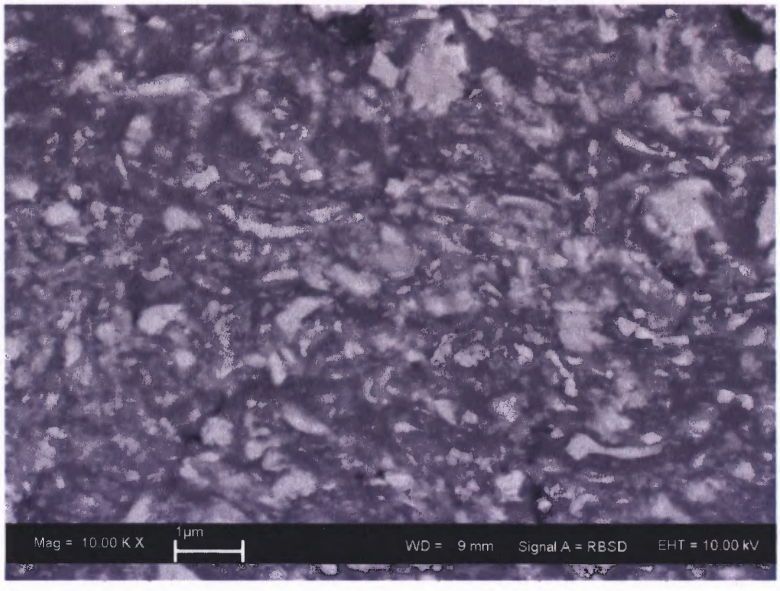

Figure 3.5 High magnification image of single particle of 8Al+3CuO nanocomposite powder.

Figure 3.6 shows an image of the powder made using the nano-sized copper oxide. The copper oxide inclusions are very small and it is difficult to distinguish individual particles. Due to the nature of nanoparticles they tend to agglomerate inside the aluminum matrix.

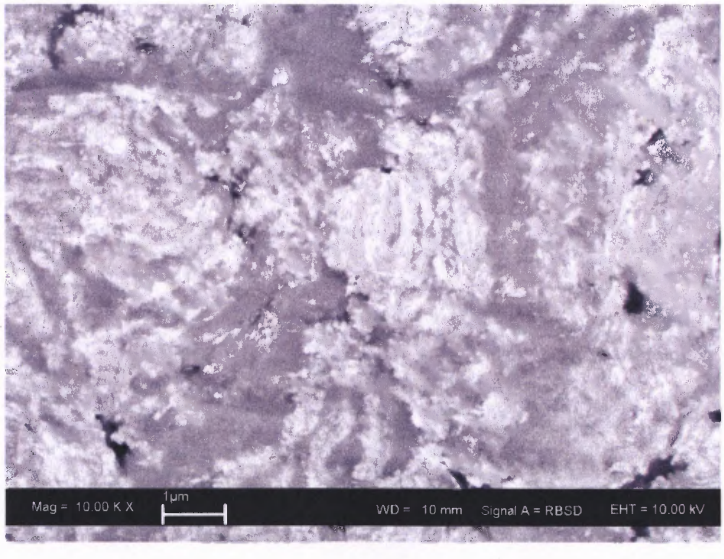

Figure 3.6 High magnification image of 8Al+3CuO nanocomposite prepared with nano-size copper oxide.

The copper oxide inclusions were further analyzed by using UTHSCSA Image Tool software. With this software the size distribution of the copper oxide inclusions could be analyzed from the SEM images.

Five images were used of the same sample, which were captured at different areas of the cross section. Each inclusion was classified according to its Feret diameter and placed into the appropriate size category. Each image was obtained at a magnification of 10 000 x. The images used are grey scale and have 255 levels of color intensity. A threshold was chosen to indicate the maximum and minimum intensities to include as a particle. Figure 3.7 shows an example of the selection of the copper oxide particles as indicated by the image on the left, where the black areas correspond to the copper oxide inclusions in the right image.

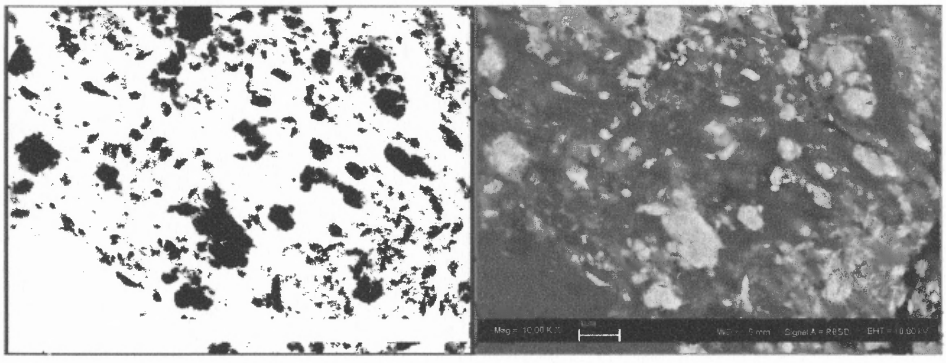

Figure 3.7 Example of threshold used to identify copper oxide inclusions from SEM images.

Care must be taken to ensure consistent threshold settings. Choosing too high a value causes the areas to overlap and indicates particles larger than they should be. Too low of a value induces error where smaller particles are omitted. Once the objects are identified, they are classified by their diameters and put into the appropriate bins. Figure 3.8 and Figure 3.9 below show the frequency as a function of particle size for the 8 mole

composition made with different milling conditions and three different compositions made using the same milling condition.

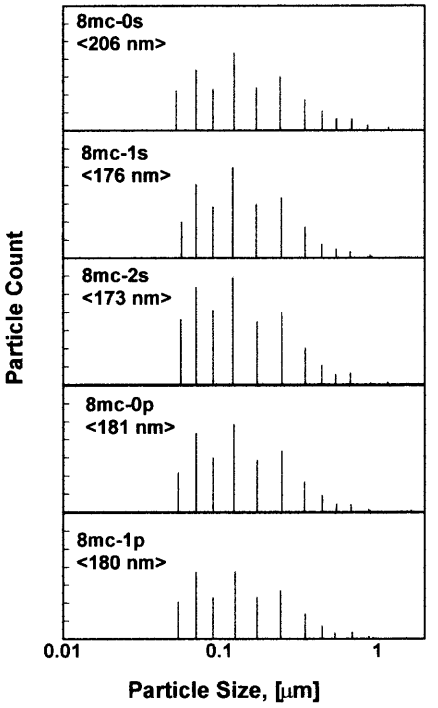

Figure 3.8 Particle size distribution of copper oxide inclusions analyzed from SEM images of different milling conditions.

Figure 3.8 shows particle size distribution functions that are very similar in shape for each milling condition. The mean inclusion size also shows little difference, with sample 8mc-0s having the largest mean. The size analysis for these samples indicates that indeed copper oxide inclusions with nanometer dimensions are fully embedded into the aluminum matrix. Samples 8mc-0p and 8mc-1p have almost identical functions, which are expected since the CuO is of the same pre-milled type.

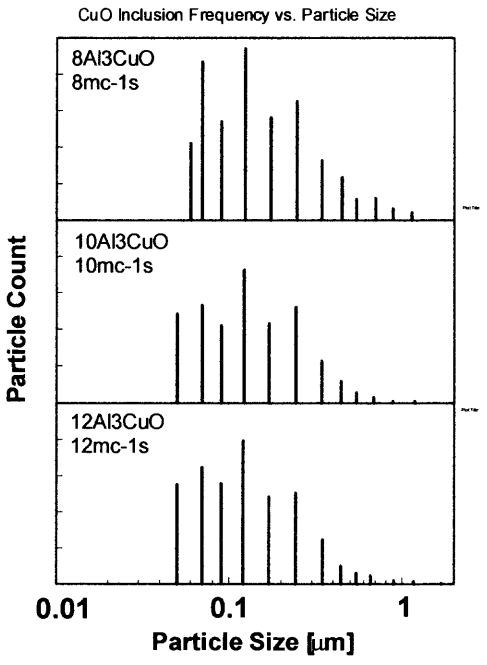

Figure 3.9 Particle size distribution of copper oxide inclusions analyzed from SEM images for three different compositions.

The size distributions for 10 and 12 mole compositions are almost identical. Almost no inclusions are found to be above 1 micron. The 8 mole composition seems to also have the highest frequency of finer particles. This can be attributed to the harder milling due to less aluminum content as compared to 10 and 12 mole. No particles are detected below 50 nm. This may be due to the resolution limit of the microscope and cannot detect particles at this level.

3.3 Composition

X-ray diffraction (XRD) was used to find evidence of partial reaction during the milling process. As a result of such reaction, formation of Cu_2O and Cu is expected which, should be detectable from the XRD patterns. In addition, formations of Al-Cu alloys are possible if free Cu is produced as a result of partial reaction.

Three patterns collected for the sample prepared using the same starting powders but with varying milling conditions are presented in Figure 3.10.

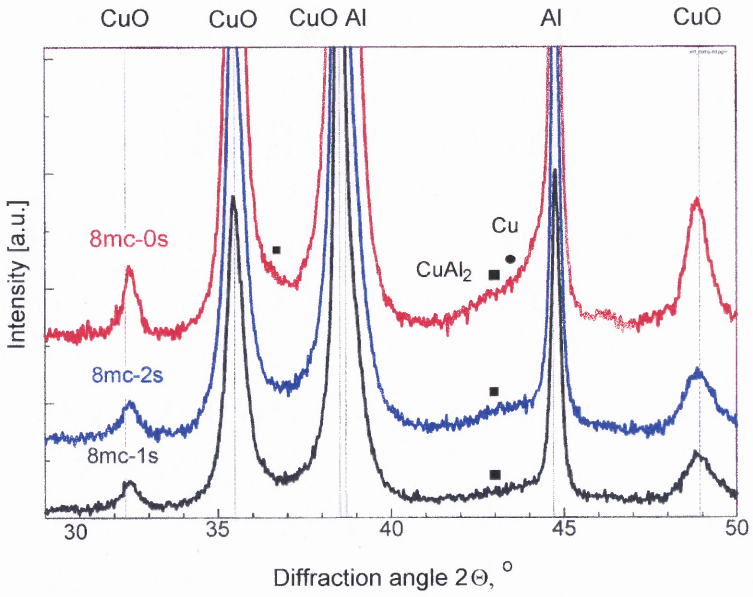

Figure 3.10 XRD patterns of 8Al+3CuO prepared using different milling conditions.

The patterns are generally similar with main peaks of aluminum and copper oxide as expected. The scale in Figure 3.10 is selected to expand the trace background where signatures from the minor phases can be observed. The background is most prominent for the 8mc-0s sample prepared with smaller amount of PCA. Based on the locations of the raised background, signatures of Cu and $CuAl_2$ can be detected. Noticeable background indicative of presence of $CuAl_2$ is also visible for sample 8mc-2s, milled for a longer time. Based on this comparison, sample 8mc-1s appears to contain the smallest amount of the partially reacted material and thus it is expected to be most reactive in the combustion tests.

A similar comparison of the XRD traces is shown in Figure 3.11, however, the milling conditions were maintained the same while the starting copper oxide powder

varied. The sample prepared using regular micron-sized powder appears to contain the smallest amount of the products of partial reaction.

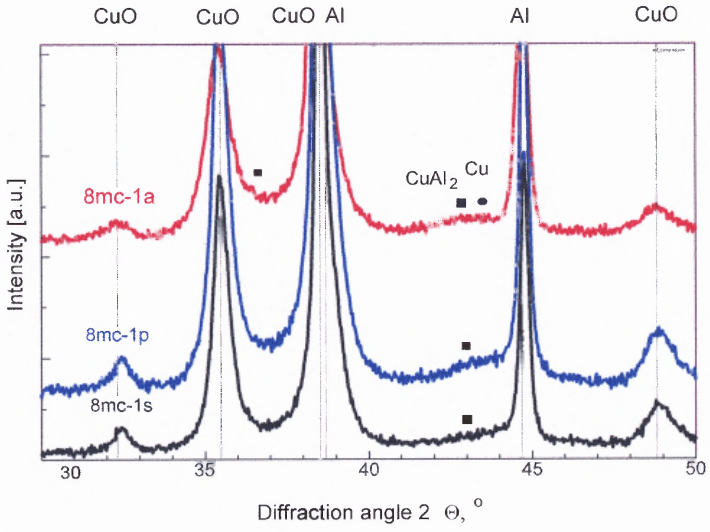

Figure 3.11 XRD patterns of 8Al+3CuO nanocomposite prepared using different copper oxide powders.

3.4 Thermal Analysis

Figure 3.12 shows the measured DSC traces for different samples of the 8Al+3CuO nanocomposite powders. The traces shown were baseline-corrected by subtracting the signal recorded during the second heating of the same sample from the signal of the first heating. Heating of all samples from room temperature to 1000 °C was accompanied by a broad and weak exothermic event between 100 and 535 °C. An endothermic peak was observed between 530 and 560 °C. This peak was, most likely, associated with eutectic melting of an Al-Cu alloy produced as a sub-product of low-temperature exothermic reaction. Indeed, as shown in Figure 3.13, eutectic in the Al-rich region of the Al-Cu phase diagram was reported [25].

As the temperature increased further, a strong exothermic peak was observed between 560 and 700 °C.

The areas of both exothermic and endothermic events observed in the DSC experiments were integrated to evaluate the overall heat effects associated with different processes. The peak areas corresponding to the subsolidus processes (from the beginning of the experiment and until the first endothermic peak), the strongest exothermic event (around 600 °C), and the total exothermic effect until about 700 °C were assessed separately. In addition, the peak area corresponding to the observed endothermic peak was also determined. The results are presented in Table 3.1. Also shown in Table 3.1 are the data from CVE experiments, specifically, the ratio of the maximum to initial pressure, P_{max}/P_{ini}, and the maximum rate of pressure rise, dP/dt_{max}, corresponding to each specific sample of 8Al+3CuO.

No direct correlation was observed between the P_{max}/P_{ini} ratio and dP/dt_{max} on one hand and the peak areas observed from the respective DSC traces, on the other. However, sample 8mc-1s exhibiting the highest values for both P_{max}/P_{ini} and dP/dt_{max}, was also characterized by the highest heat release both for the strongest exothermic peak and for the entire duration of the DSC experiment.

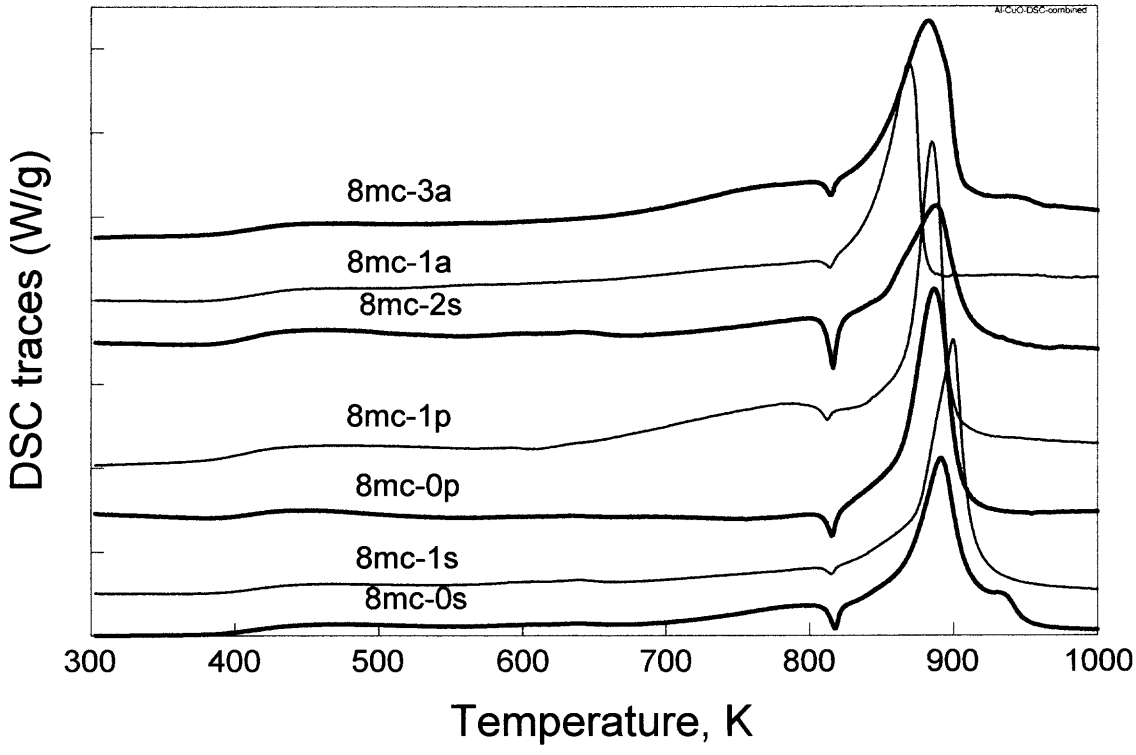

Figure 3.12 DSC traces for different milling conditions of 8Al+3CuO.

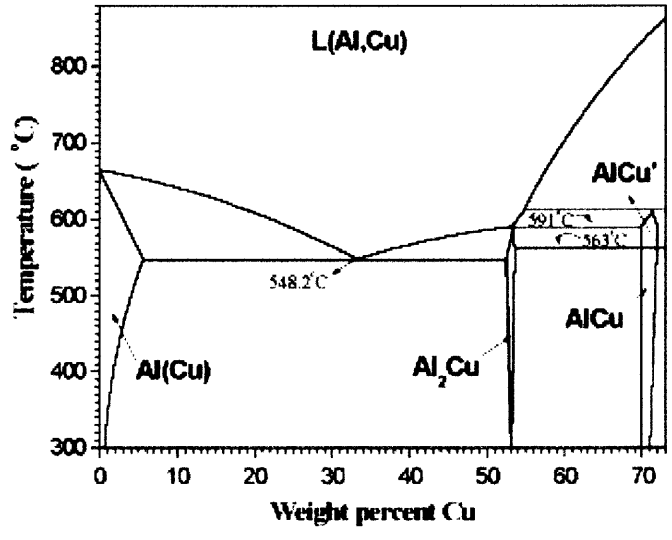

Figure 3.13 An Al-Cu phase diagram showing the Al-rich region.

Table 2.1 Table of Data From the DSC Analysis

Sample ID	DSC results				CVE results	
	Subsolidus processes (J/g)	Strongest exothermic event (J/g)	Total exotherm (J/g)	Endothermic peak (J/g)	P_{max}/P_{ini}	dP/dt_{max}, (atm/s)
8mc-0s	528	1261	1789	-24.25	3.66	20.01
8mc-1s	630	1406	2036	--3.502	4.82	78.1
8mc-0p	649	1273	1922	-22.89	4.15	59.95
8mc-1p	691	1233	1924	-10.53	4.34	45.5
8mc-2s	795	1038	1833	-52.83	4.27	32.65

3.5 Filament Ignition

A summary of results of the ignition temperature measurements is presented in Figure 3.13.

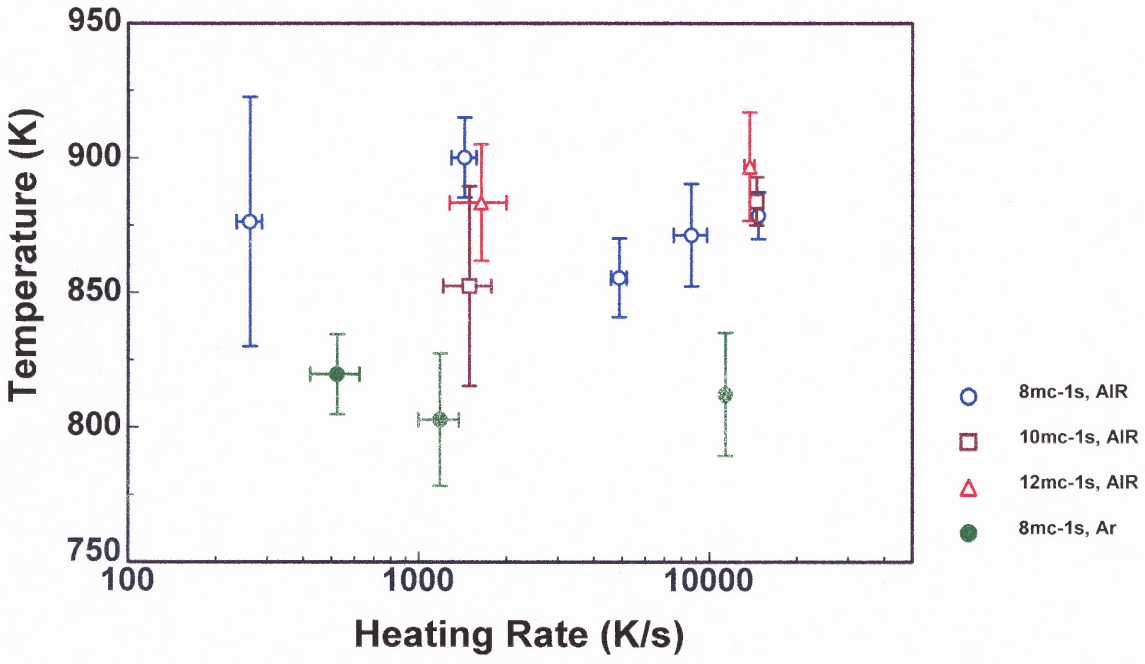

Figure 3.14 Results from filament ignition experiments for different samples under different heating rates.

Despite the variation in the heating rate from 200 to 15000 K/s, the ignition temperatures measured in air remain nearly constant for all the powders tested. The ignition temperature is also not affected significantly by the milling conditions or specific composition of the metal-rich nanocomposite xAl+3CuO powders with x varied from 8 to 12.

The experiments in argon were performed only with one powder and the measured ignition temperature was found to be lower than that in air. Once again, no effect of heating rate was observed.

Note that the measured temperature is that of a filament adjacent to the powder coated on its surface. The temperature of the igniting powder is typically somewhat higher [22]. Thus, the difference between the ignition temperature measured in argon and air are most likely explained by a lower thermal conductivity of argon which results in smaller heat losses by convection, and in smaller temperature difference between the filament and the powder. It is interesting to note the average ignition temperature for the powder in argon is 800 K which corresponds to the endothermic peak before the main exothermic reaction peak observed in the DSC experiment.

The results of measurements presented in Figure can be compared to the ignition temperature measured using the same experimental technique for stoichiometric nanocomposite powders 2Al+3CuO prepared by ARM. Several powders were prepared in [13] and the powder with the optimized milling condition was observe to ignite in air at temperatures 650-750 K; lower than the ignition temperatures shown in Figure 3.14. Furthermore, the ignition temperature for the optimized stoichiometric powder was affected by the heating rate. However, other stoichiometric powders for which the

milling conditions were not optimized, were observed to ignite in air at temperatures varied around 850-900 K which did not appear to be affected by the heating rate. These latter results directly compared to the current measurements for the metal-rich nanocomposite powders. The independence of the measured ignition temperature on the heating rate indicates that ignition could be triggered by an invariant phase change occurring at a specific temperature, as observed in the DSC experiment. The relationship of such a phase change, e.g., eutectic melting and ignition mechanism needs to be investigated further.

3.6 Combustion Performance

The results of the constant volume explosion experiments are summarized in Figure 3.15. The top plot shows the ratios of maximum explosion pressure, P_{max}, over the initial pressure in the vessel prior to ignition, P_{ini}. This ratio is generally proportional to the flame temperature of combustion. Comparison of the value of P_{max} / P_{ini} for the samples with the same bulk composition gives one a measure of the combustion efficiency. The results suggest that sample 8mc-1s demonstrates the highest efficiency among all similar samples. The plot at the bottom shows the maximum rate of pressure rise obtained from the CVE experiments. While no direct correlation between the P_{max} / P_{ini} ratio and dP / dt_{max} can be observed, the same sample that exhibited the highest P_{max} / P_{ini} ratio also shows the highest dP / dt_{max}. This same sample was also shown to contain the smallest amounts of partial reaction products shown in Figure 3.10 Therefore, based on the CVE experiments and based on the XRD analysis of the materials phase compositions, the milling conditions corresponding to the sample 8mc-1s are selected as optimized.

Samples with increased concentration of aluminum (10mc-1s and 12mc-1s) were prepared with the same milling conditions and the results of the CVE experiments for those samples are also shown in Figure 3.15. As expected, both the rate of pressure rise and the maximum pressure decrease as the amount of aluminum in the metal-rich nanocomposite powder increases.

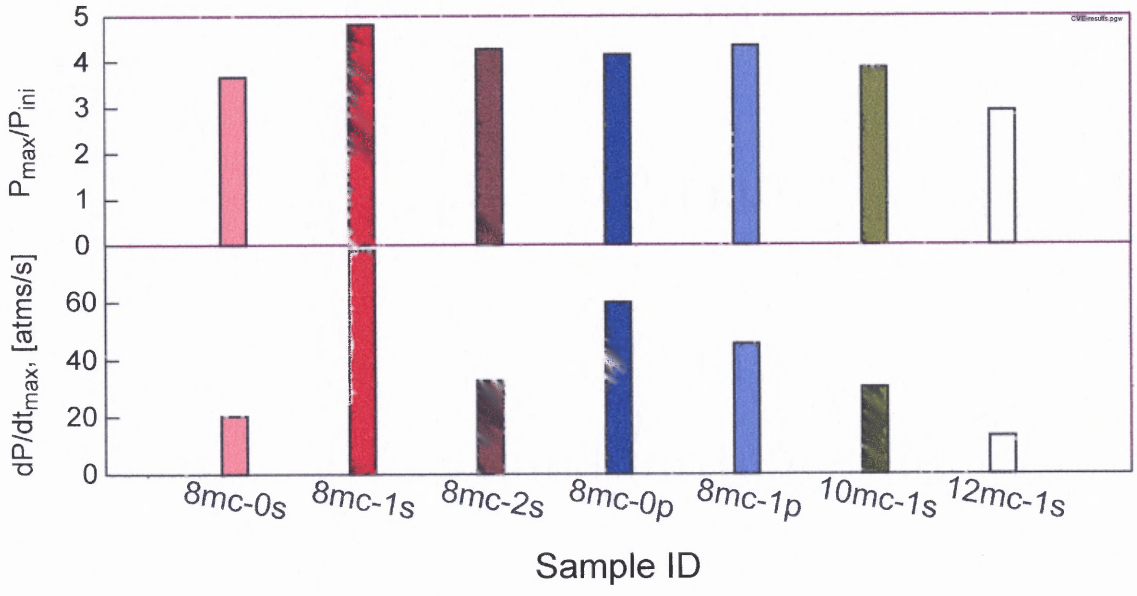

Figure 3.15 Performance results obtained from CVE experiment for different samples.

3.7 Analysis of Combustion Products

Analysis of combustion products using SEM revealed interesting information. In Figure 3.16 are shown many types of different particles formed from the combustion.

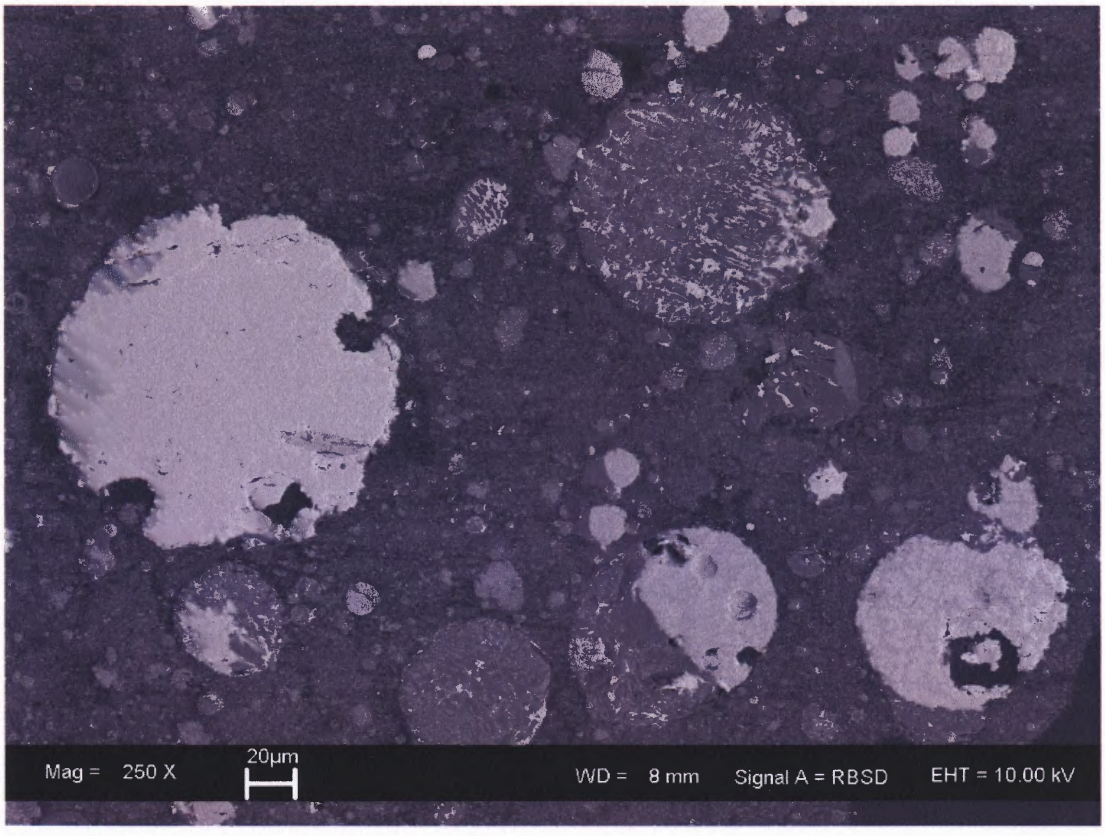

Figure 3.16 Low magnification SEM image of combustion products.

The different types of particles seen include Al-Cu alloys in various atomic ratios, mixed compositions of aluminum oxide and Cu, and smoke. Pure copper particles expected as a product are very rare. Most of it seems to have formed into alloy with the aluminum. The alloying with aluminum may be a significant factor in the observed decrease in combustion performance of the powders when the aluminum content is increased. These alloys stabilize the aluminum and thus prevent oxidation with the air. Also, they can act as heat sinks and quench the reaction resulting in incomplete burning of all the powder particles. The alloy formation may also be a significant mode of heat transfer [26].

The types of alloys formed vary, while two main compositions seem to appear more frequently. Using the EDX attachment of the SEM, one composition seems to be

60% Al and 40% Cu by atomic percent. The other composition observed was close to 50% Al and 50% Cu. Characteristic dendrite formations were detected in many cross-sectioned particles and are presented in Figure 3.17. The lighter phase (inclusions) is richer with Cu than the darker matrix. Such structures have most likely formed from a cooling molten Al-Cu solution.

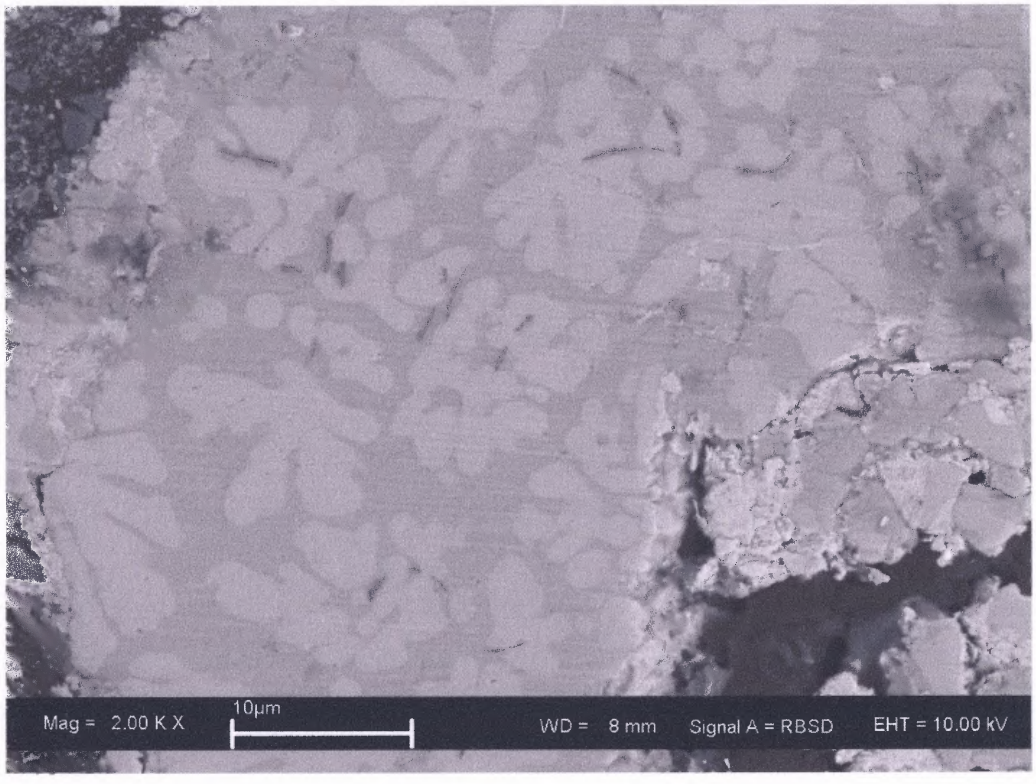

Figure 3.17 High magnification SEM image of combustion products indicating different alloy formations.

The 10 and 12 mole products had similar types of particles and alloys. The exception is that as the aluminum content of the compositions increased, the products yielded more alloys of the aluminum-rich alloys. Another observation made was the increase in the number of unburned nanocomposite particles with the increase in Al content of the starting nanocomposite powder. Figure 3.18 shows an image of the 10

mole combustion products. The arrows indicate particles which are unburned nanocomposites.

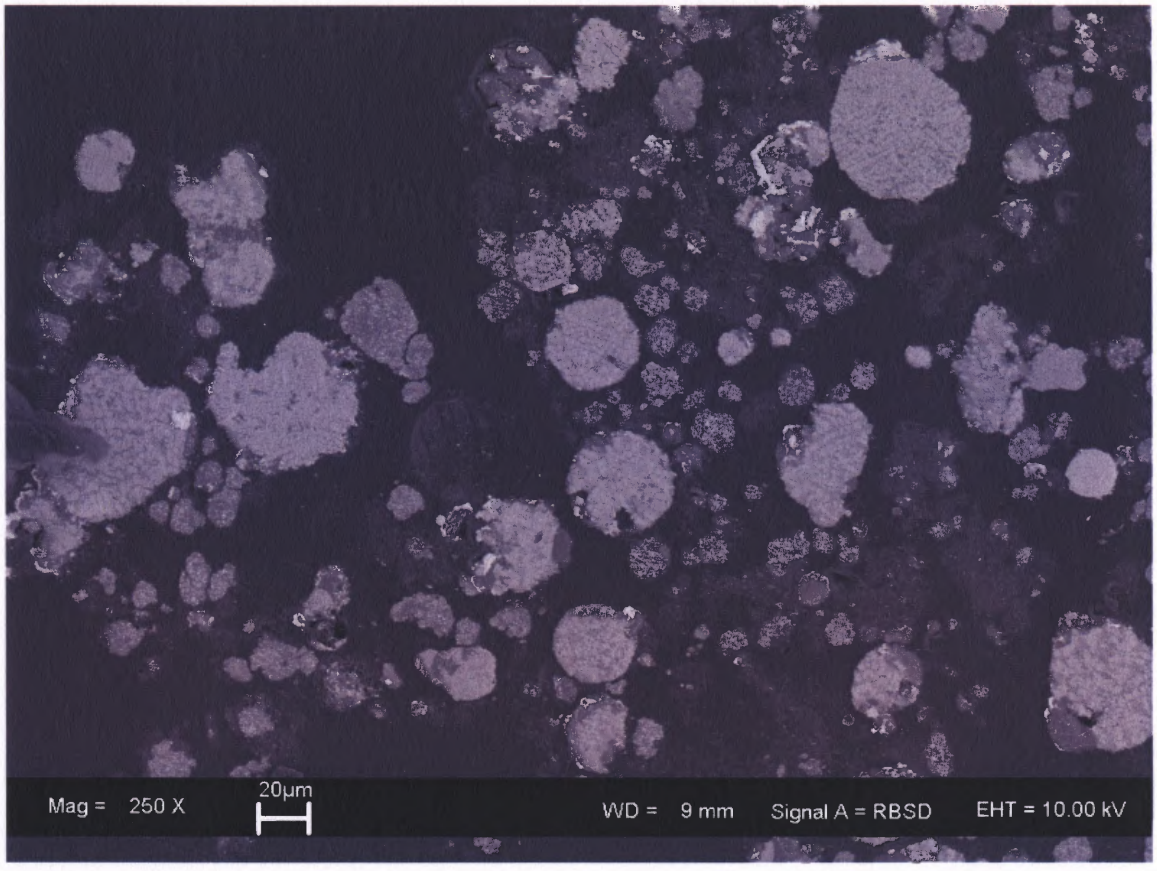

Figure 3.18 Low magnification SEM image of combustion products for 10Al+3CuO nanocomposite powder.

The size of the product particles are also noticeably large compared to the original size of the nanocomposite powders. Alloy particle as large as 200 microns were found throughout the samples. An example of these relatively huge particles is shown in Figure 3.18 above.

To further analyze the combustion products, XRD was performed for the different samples used in the CVE apparatus. The products were carefully retrieved after each combustion test and mixed thoroughly in a mortar and pestle with some solvent. This

was fully dried and used to prepare the sample for XRD. Figure 3.19 shows an example of a XRD pattern obtained for a sample.

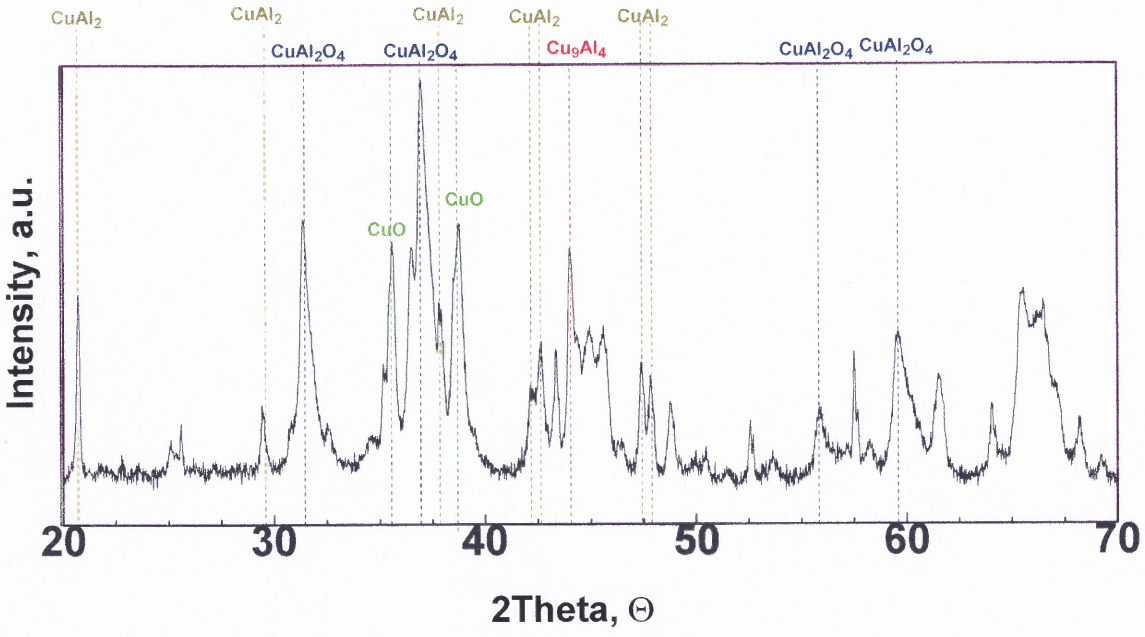

Figure 3.19 XRD pattern of combustion products for 8Al+3CuO, 8mc-1s.

Figure 3.17 indicates some of the major phases that were present in the products. The phases detected include: aluminum, Cu_9Al_4, $CuAl_2O_4$, γ-alumina, Cu_2O, CuO, $CuAl_2$, α-alumina, $Cu_2Al_4O_7$. GSAS software was used in order to fit a calculated pattern to the observed pattern by entering the structural information of each phase. Figure 3.20 shows a close view of a portion of the XRD pattern that has been refined. The black crosses indicate the points obtained experimentally, whereas the red line indicates the pattern that has been fit by calculation. Although a perfect match was not achieved, the refinement fits a pattern quite closely.

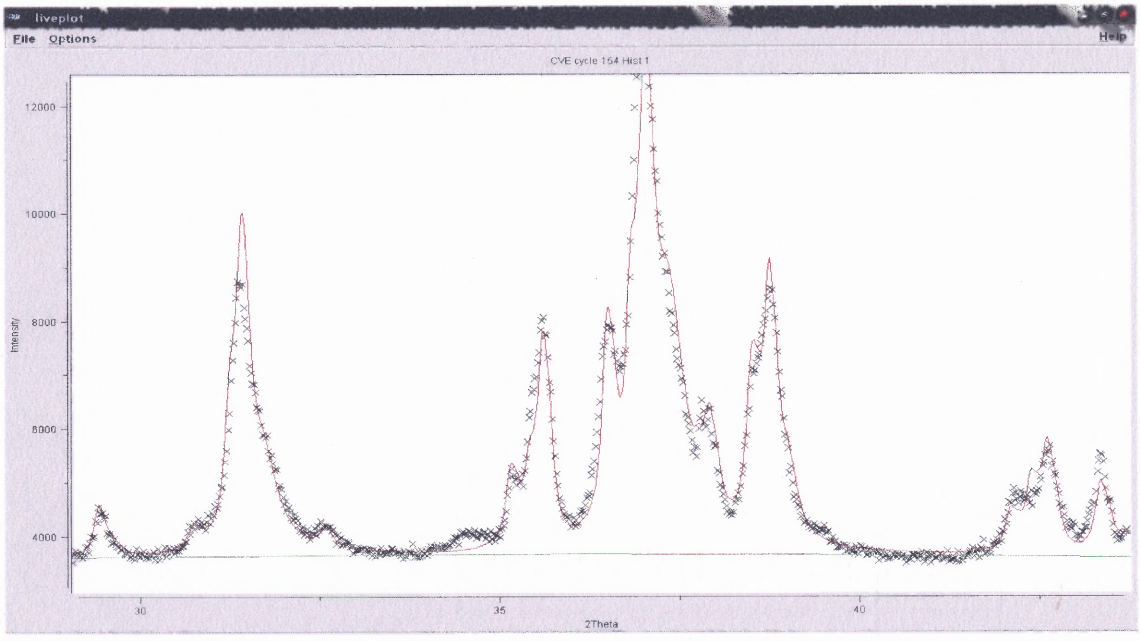

Figure 3.20 Refinement of XRD pattern using GSAS software.

Based on this refinement, the weight fraction for each phase could be calculated. Figure 3.21 shows the weight fraction of each phase as found for different samples of the combustion products. The variations between the different 8 mole compositions are not very large. An interesting observation is made with the 8mc-1s sample noting it has the lowest amount of aluminum while having the best CVE results in terms of maximum achieved pressure and the rate of pressure rise.

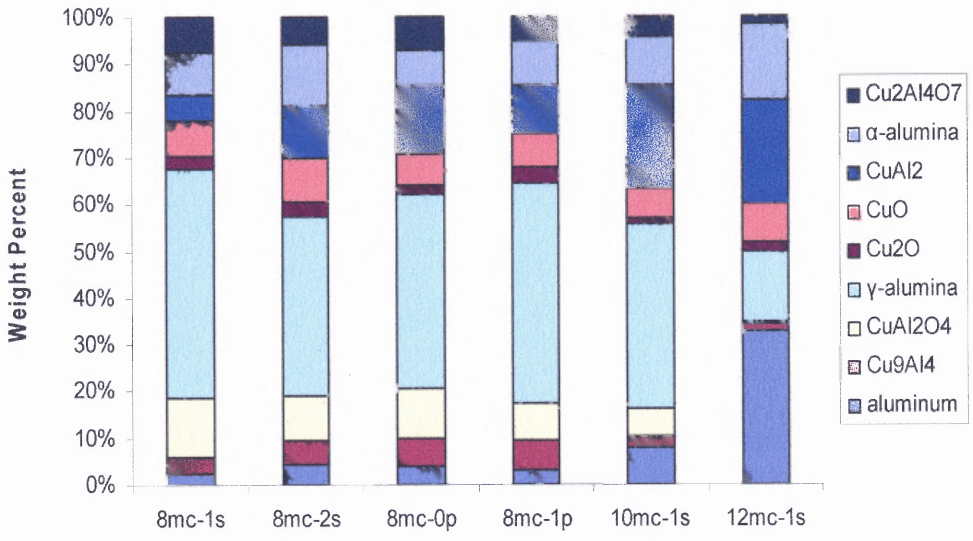

Figure 3.21 Results of XRD combustion product analysis showing weight fractions of each phase.

3.8 Joining Experiment Results

Two types of materials were employed in the joining study. The first material used was an Al-CuO nanocomposite of stoichiometric bulk composition. Bonding of plates was achieved, although the bond was rather weak. Figure 3.22 shows three sequential frames from the ignition of one of the pellets inside the experimental setup. The first frame depicts the experimental setup showing the plates held together with the spring inside the vise. The ignition filament is position on the top surface of the pellet. In the second frame the ignition filament is heating to a high temperature, and in the third frame the ignition of the pellet is observed.

Figure 3.22 Three sequential frameshots from the digital video recorder.

To examine the nature of the bond, cross sections were made of the bonded plates, and the interface was analyzed using SEM.

Figure 3.23 Low magnification SEM image of interface for plate which was bonded.

Figure 3.23 shows a typical sample interface. The dark grey area occupying most of the image is the fiberglass material of the plate. The copper foils are observed as the light colored areas. The grey material inside is aluminum oxide and the darkest material is epoxy that was used in the preparation of the sample. This image is representative of

the kind of interface observed in the different samples. There is no distinct clear connection to bridge one surface to the other. There is a large agglomeration of copper located at the interface space which is not connecting the two foils in the plane of the cross-section. It is likely that multiple formations like that have bridged the copper foils in several locations in the sample, providing a bond. However, because of the localized nature of the produced bridges, the bond was fairly weak.

Some of the copper foil is unaffected and remains intact, while elsewhere the copper foil is missing completely or replaced by aluminum oxide. The removal of the copper foil is certainly undesirable and it indicates that the local energy release exceeded that necessary for joining and was sufficient to melt the entire portion of the copper foil. Upon visual inspection of the bonded plates, it is noted that a very small amount of material remains after reaction of the thermite pellet. The reaction seems to expel most of the material considering that gas phase copper may be produced.

The metal-rich material was considered next in order to reduce the local heat (and gas) release and increase the amount of pure metal useful as filler. A similar pellet creation methodology was used in order to see if any effect was observed due to different pellet synthesis parameters. The bulk compositions used included 8, 10, and 12 mole nanocomposite powders. All plates were bonded with every sample used. SEM imaging was again used to study the bonding interface of the plates.

The best case of bonding was observed for a 10 mole pellet. Figure 3.24 shows the interface where the two copper foils are clearly in contact and some bridges are formed. The problem however is identified: the right side is detached from the fiberglass plate. In other words, while the two foils bonded to each other, one of the foils debonded

from its initial substrate. The separation of the foil from its substrate resulted in the penetration of the reaction products behind the copper foil. In this case, the typical reaction products are not pure copper and aluminum oxide as seen in the stoichiometric compositions. Different types of alloys are formed, as observed from the analysis of the combustion products from previous experiments.

Compared to the previous joining experiments that were carried out using stoichiometric material, the metal-rich compositions seem to allow more material to remain in between the interface. This was observed in both the SEM images and also upon visual inspection. The reason for this is possibly due to the presence of the excess aluminum that allows formation of the alloys. However, the reaction temperature remains too high and the continuous and uniform bonded areas are not observed.

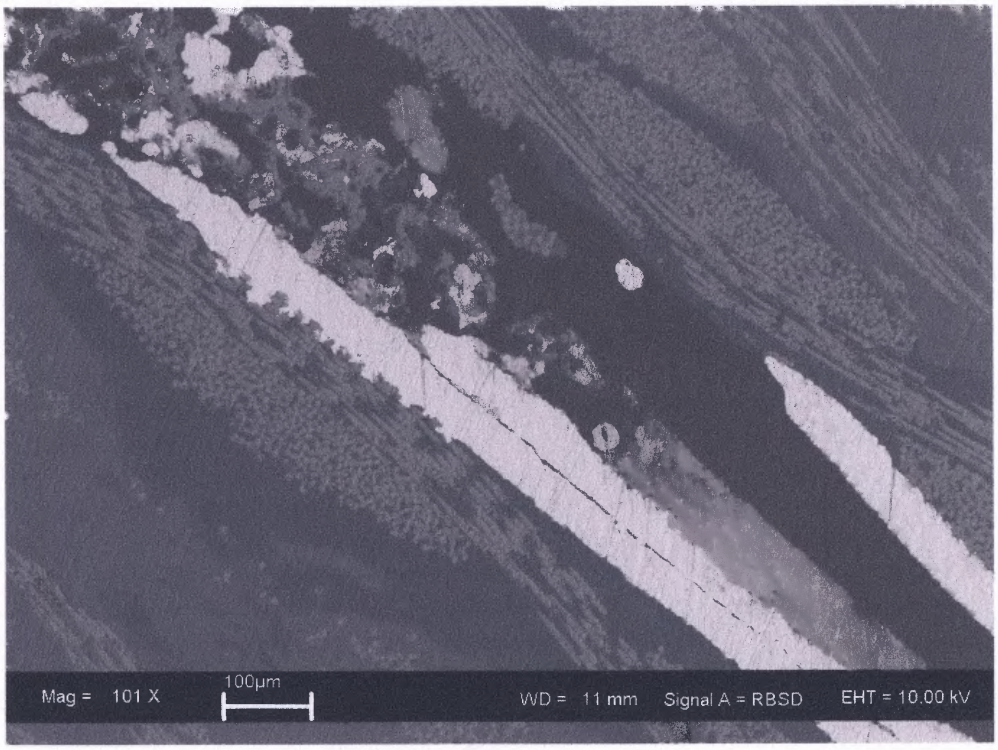

Figure 3.24 Low magnification SEM image showing interface that has some indication of bonding.

Different kinds of Al-Cu alloys were observed to have formed at the interface. Figure 3.25 shows evidence of different alloys seen to form dendrite formations within another alloy, as was observed in SEM images of combustion products from the CVE.

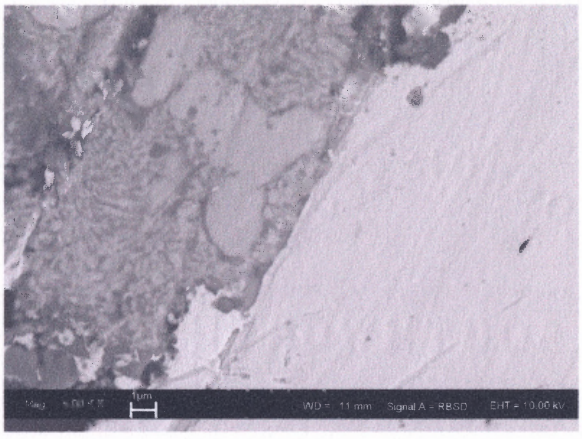

Figure 3.25 High magnification SEM image showing different types of alloys formed inside the interface.

CHAPTER 4

CONCLUSIONS

Different metal-rich nanocomposites in the thermite system Al-CuO were prepared by arrested reactive milling, characterized, and compared to one another. Based on the x-ray diffraction phase analysis and constant volume explosion experiment results, the optimized milling conditions for preparation of such powders were selected. It was also shown that the powder particle size distributions and ignition temperature are less sensitive to the specific milling conditions than the results of constant volume explosion experiments. Using nano-sized or finely divided micron-sized CuO powder as a starting material does not result in a more refined or more reactive nanocomposite powder. Instead, the concentrations of undesirable products of partial reaction (Cu, $CuAl_2$ alloy) during the ball milling increase, reducing the quality of the produced nanocomposite powder. There was no direct correlation between the measured DSC traces and the results of constant volume explosion experiments. The ignition temperature of metal-rich xAl+3CuO nanocomposites with $x \geq 8$ is 870 ± 30 K. It was not observed to change as a function of the heating rate indicating that the ignition is likely triggered by an invariant phase transition. Such a transition is detected in the DSC experiments and a related eutectic melting in the Al-Cu binary system is reported in the literature.

Compositions of the combustion products collected from CVE experiments correlate with the respective explosion pressure measurements. Generally, higher explosion pressures are detected for the samples for which less unreacted metal phases are detected in the products. A large number of Al-Cu alloys were observed to form in

the combustion products, which could affect significantly the final combustion efficiency and rates for such material systems.

The joining experiments prove the feasibility of bonding using the Al-CuO thermite pellets. However, the obtained bonds are weak and as evidenced by the SEM images not uniform. Using aluminum rich compositions for joining appears to improve the bond strength and enables to result in a larger fraction of combustion products to serve as filler material.

REFERENCES

1. Palaszewski, B., and Zakany, J.S., 1995, "Metallized Gelled Propellants: Oxygen/RP-1/Aluminum Rocket Combustion Experiments,"AIAA, 95-2435.

2. Gany, A., Netzer, D.W., 1985, "Fuel Performance Evaluation for the Solid-Fueled Ramjet," International Journal of Turbo and Jet Engines, 2 pp. 157-168.

3. Beckstead, M.W., 2006 "Recent Progress in Modeling Solid Propellant Combustion," Combustion, Explosion and Shock Waves, 42 (6), pp. 623-641.

4. Moorer, D.S., Son, S.F., Asay, B.W., 2004, "Time-Resolved Spectral Emission of Deflagrating Nano-Al and Nano-MoO3 Metastable Interstitial Composites," Propellants, Explosives, Pyrotechnics, 29 (2), pp. 106-111.

5. Bockmon, B.S., Pantoya, M.L., Son, S.F., Assay, B.W., Mang, J.T., 2005, "Combustion Velocities and Propagation Mechanisms of Metastable Interstitial Composites," Journal of Applied Physics, 98 (6), pp. 1-7.

6. Plantier, K.B., Pantoya, M.L., Gash, A.E., 2005, "Combustion Wave Speeds of Nanocomposite Al/Fe2O3: The Effects of Fe2O3 Particle Synthesis Technique," Combustion and Flame, 140 (4), pp. 299-209.

7. Prentice, D., Pantoya, M.L., Gash, A.E., 2006, "Combustion Wave Speeds of Sol-Gel Synthesized Tungsten Trioxide and Nano-Aluminum: The Effect of Impurities on Flame Propagation," Energy and Fuels, 20 (6), pp. 2370-2376.

8. Duckham, A., Brown, M., Besoin, E., Van Heerden, D., Knio, O.M., Weihs, T.P., 2004, "Metallic Bonding of Ceramic Armor Using Reactive Multilayer Foils," Ceramic Engineering and Science Proceedings, 25 (3), pp. 597-603.

9. Mann, A.B., Gavens, A.J., Reiss, M.E., Van Heerden, D., Bao, G., Weihs, T.P., 1997, "Modeling and Characterizing the Propagating Velocity of Exothermic Reactions in Multilayer Foils," Journal of Applied Physics, 82 (3), pp. 1178-1188.

10. Schoenitz, M., Ward, T.S., Dreizin, E.L., 2005, "Fully Dense Nano-Composite Energetic Powders Prepared By Arrested Reactive Milling," Proceedings of The Combustion Institute, 30 pp. 2071-2078.

11. Dreizin, E.L., Schoenitz, M., filed Nov. 2004, US Patent Application for "Nano-Composite Energetic Powders Prepared by Arrested Reactive Milling," 20060053970.

12. Umbrajkar, S.M., Schoenitz, M., Dreizin, E.L., 2006, "Control of Structural Refinement and Composition in Al-MoO3 Nanocomposites Prepared by Arrested Reactive Milling," Propellants Explosives and Pyrotechnics, 31 (5), pp. 382-389.

13. Umbrajkar, S.M., Schoenitz, M., Dreizin E.L., 2006, "Exothermic Reactions in Al-CuO Nanocomposites," Thermochimica Acta 451, pp. 34-43.

14. Takacs, L., 2002, "Self-Sustaining Reactions Induced by Ball Milling," Progress in Materials Science, 47 (4), pp. 355-414.

15. Ward, T.S., Chen, W., Schoenitz, M., Dave, R.N., Dreizin, E.L., 2005, "A Study of Mechanical Alloying Processes Using Reactive Milling and Discrete Element Modeling," Acta Materialia, 53 (10), pp. 2909-2918.

16. Y.L. Shoshin, M.A. Trunov, M. Schoenitz, X. Zhu, E.L. Dreizin, 2006, "Ignition of Aluminum-Rich Al-Ti Mechanical Alloys in Air," Combustion and Flame, 144, pp. 688-697.

17. Hertzberg, M., Cashdollar, K.L., and Opferman, J.J., 1979, "The Flammability of Coal Dust-Air Mixtures," U.S. Bureau of Mines, Rept. RI8360.

18. Cashdollar, K.L., and Hertzberg, M., April 1985, "20-L Explosibility Test Chamber for Dusts and Gases," Review of Scientific Instruments, 56 (4), pp. 596-602.

19. Cashdollar, K.L., and Chatrathi, K., 1992, "Minimum Explosible Dust Concentrations Measured in 20-L and 1m3 Chambers," Combustion Science and Technology, 87, p. 157.

20. Cashdollar, K.L., 1994, "Flammability of Metals and Other Elemental Dust Clouds," Process Safety Progress, 13, pp. 139-145.

21. Eapen, B.Z., Hoffman, V.K., Schoenitz, M., Dreizin, E.L., "Combustion of Aerosolized Spherical Aluminum Powders and Flakes in Air," Combustion Science and Technology, 176 (7), pp. 1055-1069.

22. Umbrajkar, S., Mikhaylo, T.A., Schoenitz, M., Dreizin, E.L., 2007, "Arrested Reactive Milling Synthesis and Characterization of Sodium-Nitrate Based Reactive Composites," (correspondence).

23. Lee, F.T., 2006, "Managing thermite weld quality for railroads," Welding Journal 85 (1), pp. 24-29.

24. Meric, Cevdet, and Engez, Turgut, 1999, "Understanding the Thermite Welding Process," Welding Journal, 78 (1), pp. 33-36.

25. ASM Handbook Committee, 1973, "Metallography, Structures and Phase Diagrams," Metal Handbook, OH, p. 259.

26. Son, S.F., Asay, B.W., Foley, T.J., Yetter, R.A., Wu, M.H., Risha, G.A., 2007, "Combustion of Nanoscale Al/MoO3 Thermite in Microchannels," Journal of Propulsion and Power, 23 (4), pp. 698-706.